INVITED PAPER

Laser additive manufacturing of powdered bismuth telluride

Haidong Zhang[a)]
Department of Mechanical & Aerospace Engineering, The George Washington University, Washington, District of Columbia 20052, USA

Dean Hobbis and George S. Nolas
Department of Physics, University of South Florida, Tampa, Florida 33620, USA

Saniya LeBlanc[b)]
Department of Mechanical & Aerospace Engineering, The George Washington University, Washington, District of Columbia 20052, USA

(Received 27 July 2018; accepted 25 September 2018)

Traditional manufacturing methods restrict the expansion of thermoelectric technology. Here, we demonstrate a new manufacturing approach for thermoelectric materials. Selective laser melting, an additive manufacturing technique, is performed on loose thermoelectric powders for the first time. Layer-by-layer construction is realized with bismuth telluride, Bi_2Te_3, and an 88% relative density was achieved. Scanning electron microscopy results suggest good fusion between each layer although multiple pores exist within the melted region. X-ray diffraction results confirm that the Bi_2Te_3 crystal structure is preserved after laser melting. Temperature-dependent absolute Seebeck coefficient, electrical conductivity, specific heat, thermal diffusivity, thermal conductivity, and dimensionless thermoelectric figure of merit ZT are characterized up to 500 °C, and the bulk thermoelectric material produced by this technique has comparable thermoelectric and electrical properties to those fabricated from traditional methods. The method shown here may be applicable to other thermoelectric materials and offers a novel manufacturing approach for thermoelectric devices.

I. INTRODUCTION

Thermoelectric devices offer the potential for many energy efficiency improvements because they enable solid state energy transfer and conversion. Thermoelectric materials, usually semiconductors, can directly convert thermal to electrical energy and vice versa. There are two types of applications for thermoelectric devices. Thermoelectric refrigerators use electricity for solid-state cooling via the Peltier effect, and thermoelectric generators convert heat into electricity through the Seebeck effect. Although thermoelectric materials and devices have seen extensive development since the 1950s,[1–9] two factors still hinder their proliferation: low energy conversion efficiency,[10,11] and the complexity of traditional manufacturing techniques.[12]

There has been significant effort to improve thermoelectric materials' properties because of the materials' low energy conversion efficiency. The thermoelectric material performance is usually evaluated through the thermoelectric figure of merit,[13] a dimensionless value $ZT = (S^2\sigma/k)T$, where S is the Seebeck coefficient, σ is the electrical conductivity, k is the thermal conductivity, and T is the temperature. A high ZT translates into better performance of the thermoelectric device. Substantial research has therefore been conducted on materials—from bulk to films, nanowires, and quantum dots—to increase the ZT values of materials.[14–20] However, the latter challenge, namely the device fabrication technique, has not caught up with the development of materials and the requirement for construction of complex thermoelectric structures. Traditional thermoelectric device manufacturing has multiple steps—ingot pressing or sintering powders, dicing and polishing, metallization, leg dicing, and interconnect and braze/solder application—before module assembly can even begin. This process is time consuming, wastes material, and does not allow for complex geometry fabrication. These traditional material fabrication techniques are therefore a bottleneck in expanding the application of thermoelectric technology. In fact, materials improvements have largely been limited to laboratory-scale demonstrations, while device-level improvements continue to be limited by processing and device engineering difficulties.[12]

Selective laser melting (SLM), also known as laser powder bed fusion, is an additive manufacturing process using a laser beam to selectively melt powder particles and build up parts layer-by-layer. Compared to traditional manufacturing methods, SLM is a material-efficient

Address all correspondence to these authors.
[a)]e-mail: haidongzhang@gmail.com
[b)]e-mail: sleblanc@gwu.edu
DOI: 10.1557/jmr.2018.390

one-step process that enables the fabrication of complex three-dimensional structures. In addition, depending on the specific application, the SLM process could also reduce device manufacturing and assembly time. Since its invention in the late 1980s,[21] SLM has been applied to metals,[22] polymers,[23] and ceramic materials.[24] Application examples in the medical and industrial fields include medical scaffold, dental implant, micro-tooling, aircraft engine turbine blade, bespoke filter, light-weighted thin wall hydraulic structures, etc.[25] SLM has recently been demonstrated on thermoelectric materials, with preliminary reports describing the formation of single melt tracks in bismuth telluride (Bi_2Te_3) powder compacts.[26–28] Recently, slurry-based[29–31] laser melting of multiple $Bi_2Te_{2.7}Se_{0.3}$ layers and extrusion-based[32] 3D printing of $Bi_{0.5}Sb_{1.5}Te_3$ were reported. The former used lubricants to form slurries and enables layer-by-layer spreading of the power material, and the latter adopted binder-mixed inks for particle deposition. The preparation of a high-quality slurry or ink with proper viscosity is an essential requirement for those processes; a post-process annealing, a pre-sintered bulk substrate, or a binder material was also required. Even though a sintering aid was used to fill void spaces, the final bulk of $Bi_{0.5}Sb_{1.5}Te_3$ only showed a density of 3.91 g/cm^3 (about 57% relative density).[32] Bulk samples from the ink-based process also underwent about 20% shrinkage in both width and thickness after post-process annealing.[32] The above challenges may be overcome using powder-based processes. Commercial SLM processes typically use loose powders, so adding a lubricant hinders the integration of thermoelectric material systems into a somewhat established manufacturing process. Selectively melting loose powder in a layer-by-layer approach would improve the viability of commercial SLM for thermoelectric materials and devices.

In this paper, we report the first demonstration of a successful SLM process on loose powders of thermoelectric material without any pre- or post-processing, preforming a substrate, or binder materials, so the process described herein may be directly applied in standard, commercial SLM equipment. Bi_2Te_3 powder was chosen not only because it is a standard thermoelectric material[1] but Bi_2Te_3 alloys also continue to be among the best and most widely used thermoelectric materials for both thermoelectric refrigeration and power generation for moderate temperature heat sources.[33] Bi_2Te_3 is a narrow gap semiconductor,[34] and it has also been of recent interest because it exhibits topological insulator behavior.[35]

II. EXPERIMENTS AND METHODS

The SLM process was conducted with a custom-built tool to enable flexibility in materials processed. (Commercial tools are typically specified for only a few materials such as stainless steel and titanium while our system allows for maximum flexibility for research purposes.) Bi_2Te_3 powders (99.98% trace metal basis, Alfa Aesar, Karlsruhe, Germany) were evenly spread and flattened inside a thin stainless steel ring (McMaster-Carr, Robbinsville, NJ, part number 97022A331) which serves as the powder bed container for one layer. For each layer, a laser scanned the surface in a pre-designed pattern. The laser processing was conducted in an enclosure purged with N_2 gas. An oxygen sensor monitored the oxygen level throughout the experiment, with levels maintained at or below 4%. The laser is a 1070 nm diode-pumped Ytterbium fiber laser, operating in the continuous wave mode with output power up to 100 W (IPG Photonics, Oxford, MA, YLR-Series). The system is equipped with a mid-power scanner (IPG Photonics, P30 series) to control laser beam position. After one layer was processed, another ring was added on top, and a second powder layer was deposited inside the new ring. Then the laser repeated the scan pattern. The stacked rings eventually formed a sample holder for the desired number of additive layers. The total thickness for each layer was about 150 μm. After 8 layers, an ingot in the desired shape with a thickness over 1 mm was formed.

Control samples were made using a hot press. Two sets of the original Bi_2Te_3 powders (approximately 2 grams each) were hot pressed at 500 °C in a nitrogen environment at 150 MPa. The first powder sample was hot pressed for 10 min and resulted in a sample density of 6.1 g/cm^3 (~79% relative density), and the second, hot pressed for 3 h, resulted in a density of 7.1 g/cm^3 (~92% relative density).

Phase identification was conducted with X-ray diffraction, and sample imaging was performed with scanning electron microscopy. The SLM-processed samples were first gently crushed and ground into powder using a mortar and pestle. Then powder XRD was performed with a Rigaku Miniflex II Cu K_α X-ray diffractometer (Rigaku, The Woodlands, Texas). Other SLM-processed samples were cast in epoxy resin, ground, and polished to reveal the cross section along the build direction. The surface was polished down to a 40 nm finishing using an Allied High Tech Multiprep polishing system. The SEM micrographs for the cross section were then obtained with an FEI Talos Teneo LV FEG scanning electron microscope (FEI, Hillsboro, Oregon).

The density was measured using a Mettler Toledo XS204 density determination kit (Mettler Toledo, Columbus, OH), based on Archimedes' principle. The sample was first weighed in air; then it was completely immersed in liquid and weighed again. The density was determined through the formula: $\frac{A}{A-B} \times (\rho_1 - \rho_2) + \rho_2$, where A is the sample weight in air, B is the sample weight in liquid, ρ_1 is the density of liquid, and ρ_2 is the density of air (0.0012 g/cm^3). Technical grade distilled

water was used; it has a density of 0.99764 g/cm^3 at the measured temperature of 22.7 °C.

The absolute Seebeck coefficient, S, and electrical resisitivity, ρ, were characterized in the in-plane direction. At room temperature, steady-state S and four-probe ρ were measured using a custom-designed probe, calibrated using standards and compared with a separate probe,[36,37] with an uncertainty of approximately 15% for both S and ρ. The high-temperature S and ρ were measured from 50 up to 500 °C in a He environment using a commercial Linseis LSR-3 Seebeck coefficient and electric conductivity measurement unit (Linseis Gmbh, Selb, Germany).

The specific heat c_p and thermal diffusivity λ were measured in the cross plane direction from 30 to 500 °C in vacuum using a commercial Linseis Laser Flash Analyzer (LFA 1000) with a Diode-pump IR Laser and LN_2-cooled IR detection system (Linseis Gmbh, Selb, Germany). The thermal conductivity k was determined using $k = c_p\rho_m\lambda$, where ρ_m is the mass density. The measured density value at room temperature was used for all temperatures to calculate thermal conductivity. The temperature-dependent thermal properties were measured in the direction perpendicular to that in which the Seebeck coefficient and electrical resistivity were measured due to restrictions in the measurement technique and sample geometry. Any anisotropy in thermal conductivity is not captured in the characterization results presented here. This is a common limitation encountered in thermoelectric property characterization, particularly for thin/thick film or small samples.

III. RESULTS AND DISCUSSION

The loose powders of Bi_2Te_3 were successfully processed in a layer-by-layer approach to produce a final disc-shaped part which was 8 mm in diameter and over 1 mm thick. The disk was formed with eight layers of powder with each layer about 150 μm thick. To form the disk, the optimal laser power, spot size, scan speed, and hatch distance were 25 W, ~50 μm, 500 mm/s, and 37.5 μm, respectively. These parameters led to a laser energy density E of 1.3 J/mm^2, according to $E = \frac{p}{vh}$, where p is the laser power, v is the scan speed, and h is the hatch distance.[38] The processing parameters were chosen such that the energy density was high enough to melt each layer thoroughly and low enough to avoid sample bending.

Improving density (or minimizing porosity) of the produced parts is a major challenge for SLM, regardless of whether it is applied to metals, ceramics, or semiconductors. Size distribution and particle morphology affect the ability of the powder to flow,[39–41] which influences packing of the powder bed and thus affects density (or porosity). For the case of Bi_2Te_3, the as-received powders had a large size distribution ranging from below 10 μm to larger than 150 μm, and the powder particles generally have irregular shapes (i.e., aspherical, high aspect ratio). Detailed powder characterization including size and morphology (e.g., aspect ratio and circularity) was reported previously.[42] The large size distribution and irregular particle shapes cause mechanical interlocking and lead to voids which cause low packing density of the powder bed before melting.[42] Consequently, the Bi_2Te_3 disks formed were not fully dense, as shown in Fig. 1(b). To increase density, we increased the laser power from 16 W to 25 W (changing the energy density from 0.85 J/mm^2 to 1.3 J/mm^2, respectively) with other parameters the same, resulting in an effective improvement of the density from 6.27 g/cm^3 to 6.81 g/cm^3, or 81%–88% relative density when compared to the standard Bi_2Te_3 density, 7.74 g/cm^3.[43] A comparison of the samples made with low and high energy density is shown in Figs. 1(b) and 1(c). Figures 1(b)–1(d) show multiple geometries, disc and rectangular, made with the SLM process.

The high density sample [shown in Fig. 1(c)] was further analyzed to demonstrate the quality of melting in the SLM processing. Figure 2 shows a scanning electron micrograph of the sample's cross section, in-plane along the build direction (perpendicular to the laser scan direction). No separation between adjacent layers was visible across the entire surface of the cross section. The surface features some spherical pores, the majority of

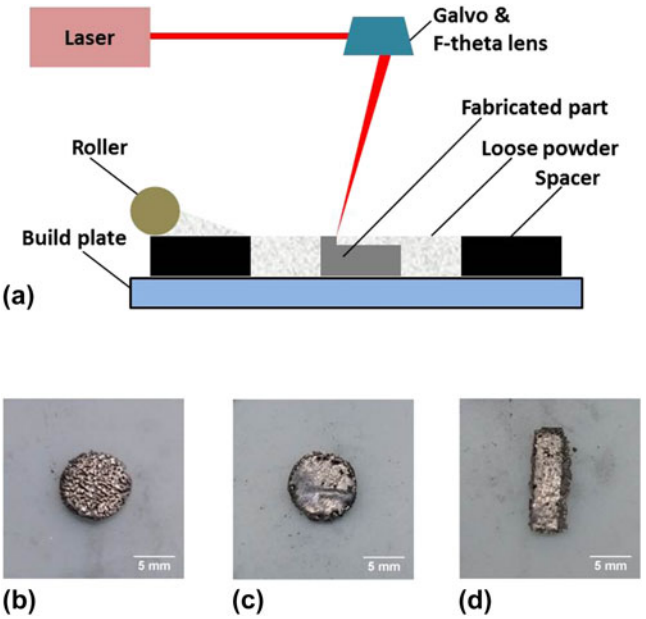

FIG. 1. Optical images of parts built from commercially available Bi_2Te_3 powder using a layer-by-layer SLM approach. (a) Sketch of the SLM process on TE materials. (b and c) Parts in disk shape, with 8 mm in diameter. (d) Part in rectangular shape ~3 mm × 11 mm. All parts are over 1 mm thick. The laser processing parameters were adjusted to increase the relative density. (b) 16 W of laser power resulted in a relative density ~81%. (c) 25 W of laser power resulted in a relative density ~88%.

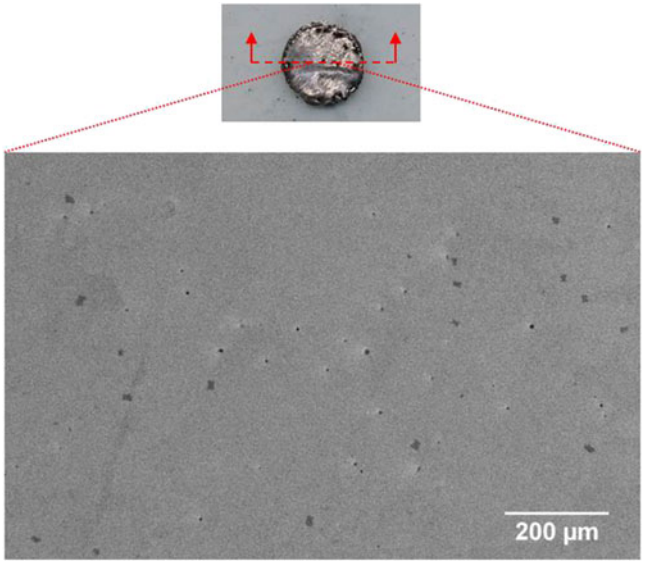

FIG. 2. Scanning electron micrograph of a polished cross section of the SLM processed Bi_2Te_3 bulk sample. Each layer is about 150 μm thick; no separation between powder layers is observable.

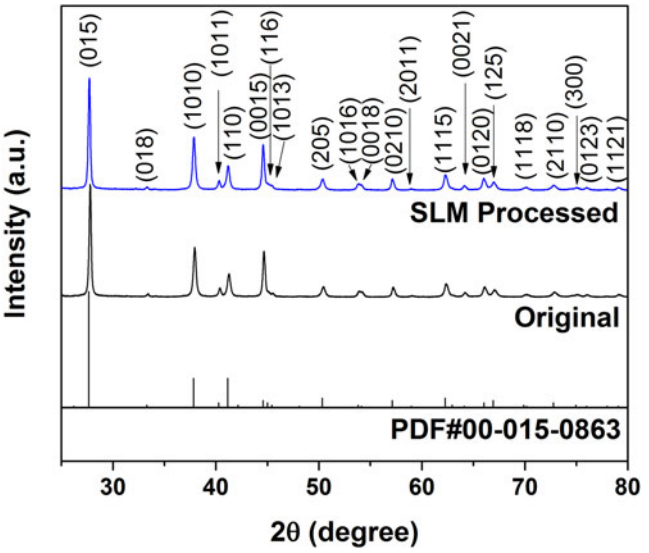

FIG. 3. XRD patterns of Bi_2Te_3 samples for original powders and those from SLM processed sample. Both spectra are well-matched with positions and intensities, and they match the database values for Bi_2Te_3 (PDF#00-015-0863).

which are approximately 5 μm or larger in diameter. Spherical pores are generated from gas trapped during rapid solidification[28,44,45] or keyhole instability and collapse.[46,47] This sample's relative density, 88%, is comparable to the control samples manufactured using hot pressing on Bi_2Te_3 (92% relative density), suggesting that the fusion of powders was quite successful through the SLM process.

To explore any chemical or structural transition during the SLM processing, the processed samples were compared to unprocessed control samples using powder XRD. The results presented in Fig. 3 indicate that the two spectra are almost identical in the measured range, and no clear new phases were observed. Both spectra are well-matched with the database values for Bi_2Te_3 (PDF#00-015-0863), suggesting the SLM process preserved the structure for Bi_2Te_3. This result is consistent with the Bi–Te system's phase diagram where the only possible phase crystallized from the liquid phase at 60 at.% of Te is Bi_2Te_3 at 585 °C.[48] XRD peak intensity differences for Bi_2Te_3 from spark plasma sintering, rolling, and forging were previously reported and interpreted as crystallographic preferred orientation changes.[49–51] However, our results do not indicate a change in preferred orientation. We did notice XRD intensity differences from coarse powders crushed from SLM processed samples, indicating a lack of random orientation. However, continuing to grind samples to fine powders led to intensities which were well-matched to the control samples, suggesting that the SLM process does not influence the intrinsic anisotropy for Bi_2Te_3.

We also characterized the thermoelectric and electrical properties of the SLM-produced samples. The room temperature Seebeck coefficient, S, and four-probe electrical resistivity, ρ, were measured in the in-plane direction using a custom-designed vacuum probe. The range of S and ρ values are 85–189 μV/K from five samples and 1–15 mΩ cm from four samples at room temperature, respectively, with the majority falling between 144 and 189 μV/K and 1–5 mΩ cm. A summary of the Seebeck coefficient and electrical resistivity values is shown in Fig. 4. The measured values vary from sample to sample, and the variation is possibly related to varying powder bed layers and defect conditions (as discussed below) which are introduced from the melting and solidification process. The aspherical powder particle morphology leads to variation in the surface condition of each powder bed layer, so there may be a slight variation in the density and porosity of the produced samples. These geometric variations affect the calculations of intrinsic physical properties since only extrinsic properties are measured (e.g., electrical resistivity is extracted from a measurement of electrical resistance). Production and selection of only spherical powder particles could narrow the variation. Our results are consistent with reported experimental values, which range from 130 μV/K to 260 μV/K for Seebeck coefficient and 0.6 mΩ cm to 2.5 mΩ cm for electrical resistivity.[52] For example, our sample with room temperature S and ρ values of 166 μV/K and 1 mΩ cm, respectively, is in good agreement with the reported values of 160 μV/K and 0.7 mΩ cm on regular p-type Bi_2Te_3 materials.[33]

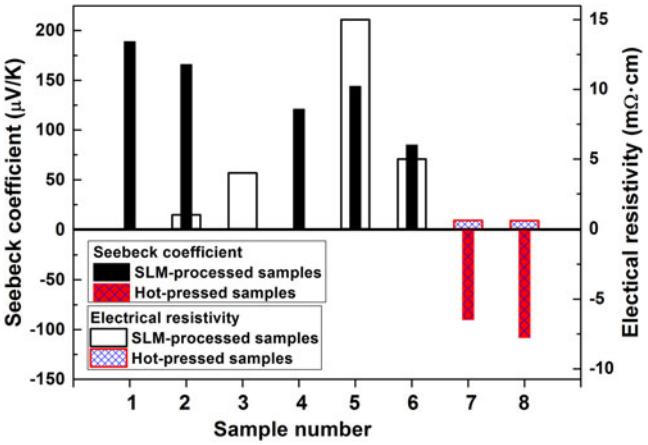

FIG. 4. A summary of the measured Seebeck coefficient and electrical resistivity at room temperature. Samples #1–#6 are the SLM-processed samples; samples #7 and #8 are fabricated through hot-pressed method on pristine powders. The processing parameters for all the samples can be found in Table S1 in the Supplementary Material.

The thermal and electrical properties of the SLM-produced samples were further characterized at high temperatures. The temperature-dependent absolute Seebeck coefficient, electrical conductivity, specific heat, thermal diffusivity, thermal conductivity, and thermoelectric figure of merit *ZT* were characterized up to almost 500 °C in either vacuum or a helium environment using the Linseis system; the results are shown in Figs. 5 and 6. The sample measured at high temperature (yielding the data in Fig. 5) was not the same sample as that measured at room temperature, but all samples were processed in the same way. The absolute value of the Seebeck coefficient is representative of the material's ability to convert thermal energy to electrical energy. As temperature increased, *S* first decreased from about 165 μV/K at 50 °C until it reached close to zero at about 350 °C. Then, the Seebeck coefficient's absolute value increased with temperature, up to −50 μV/K at 473 °C. The electrical conductivity shows a similar behavior, initially decreasing and then increasing around 300 °C.

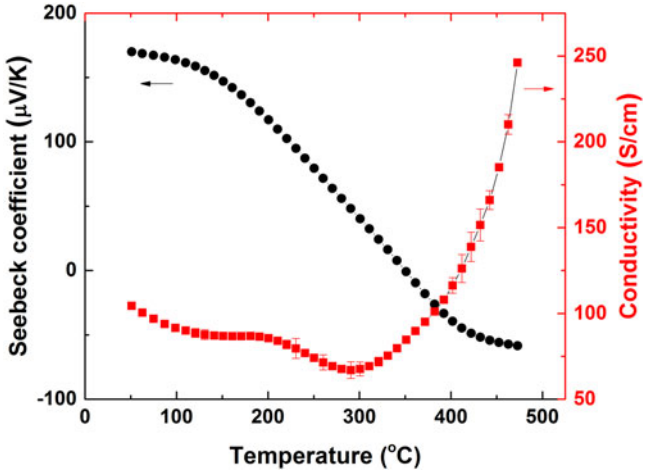

FIG. 5. The absolute Seebeck coefficient and electrical conductivity from 50 to 473 °C for the SLM-processed Bi_2Te_3 sample. The conductivity data were averaged over a set of ten measured values, and the uncertainty bar shown is from the standard deviation. The uncertainty on the measured Seebeck coefficient is ±7%, according to the Linseis technical specifications.

Both the thermoelectric and electrical behaviors are in agreement with previous reports. Unlike thin films which can be p-type or n-type,[53–55] both single crystals and polycrystalline bulk samples of Bi_2Te_3 are p-type at room temperature[48,52,56–58] if the sample is grown slowly from a stoichiometric melt without intentional doping. There are consistent reports that Bi_2Te_3 bulk samples undergo a p-to-n conversion while heated at high temperatures if the annealing time is short (less than 4 h, e.g., Ref. 59). The magnitude of the negative *S* values increases as the temperature increases,[56,60] which is consistent with our results (see Fig. 5). Even thin film samples which are n-type at room temperature show the same trend: an increasingly negative *S* and ρ that first increases and then decreases with increasing temperature.[55]

There are differing perspectives about the cause of the p-to-n transition. One theory explains the transition based on crystalline vacancy defects.[59] Point defects act as donors or acceptors depending on their energy level relative to the Fermi level. In this theory, tellurium vacancies are the electron donors and the predominant active point defects in the Bi_2Te_3 system. The original p-type material is driven to n-type because the higher temperature effectively generates additional Te vacancies for short-time heating. The conversion from p- to n-type reflects the relative concentrations and position of the Te and Bi vacancy energy levels. George et al. also suggested that an increase of vacancy concentration, due to both thermal excitations and sintering effects,[61] will result in a n-type material because the vacancies act as hole traps.[60] The idea of vacancies in Bi_2Te_3 playing a significant role was supported by several studies.[62–67] However, Hashibon and Elsässer[68] suggested that antisite defects, Te_{Bi} and Bi_{Te}, instead of vacancies, play a dominant role in the electrical and thermoelectric properties of Bi_2Te_3. The antisite defect Bi_{Te} leads to p-type conduction as an acceptor, and Te_{Bi} leads to n-type conduction as a donor. The authors also rationalized the original formation of p-type Bi_2Te_3 by claiming that there are more Te sites than Bi sites in the lattice (3:2 ratio), so the excess of Bi_{Te} defects leads to p-type semiconducting behavior. Kim et al.[55] explained their experiment results using this antisite defect model.

In summary, changes in electrical and thermoelectric properties can occur in binary compounds like Bi_2Te_3, depending on the thermal history of the material.[59]

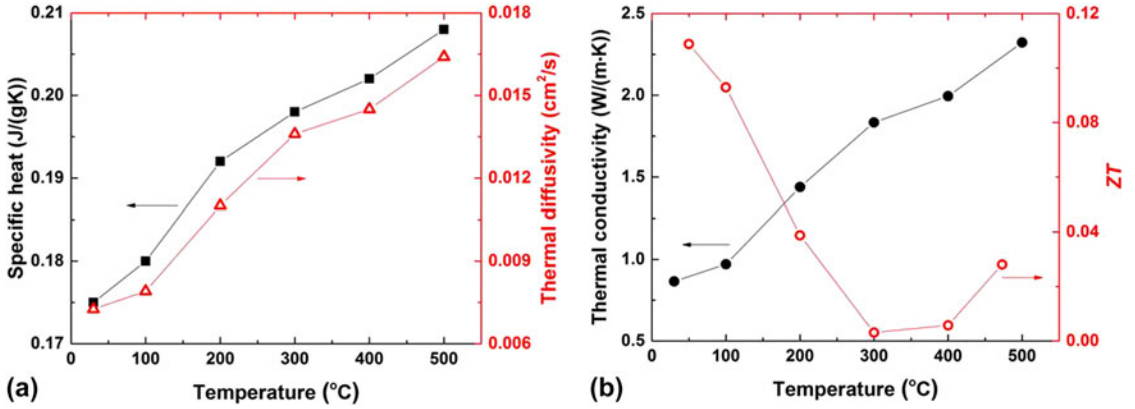

FIG. 6. The thermoelectric properties for the SLM-processed Bi_2Te_3 sample from 30 up to 500 °C. (a) Both the specific heat (square) and thermal diffusivity (triangle) increase with increasing temperature in the measured temperature range. The uncertainties for specific heat and thermal diffusivity are ±5% and ±2.4%, respectively, according to the Linseis technical specifications. (b) As the temperature increases, the thermal conductivity (filled circle) increases, and the thermoelectric figure of merit, *ZT* (open circle), first decreases until 300 °C then increases.

Although there are different explanations, a common theme is the electrical and thermal behavior of Bi_2Te_3 depends heavily on crystalline point defects, be they vacancy defects, antisite defects, or other types of point defects. To identify which effect dominates is beyond the scope of this work; however, we propose a general framework to explain our experimental results. The original sample is p-type with holes as the majority carriers. As temperature increases, increasing point defects act as donors until the material eventually becomes n-type. During this process, the material experiences a carrier density decrease from the annihilation of the promoted electrons and existing holes. The large decrease in the carrier concentration is accompanied by a slight increase in the carrier mobility, as supported by the findings of other studies.[55,69] The end effect is an increase in ρ with the initial increase of temperature, as shown in Fig. 5. As the temperature further increases to above 300 °C, the mobility of carriers sharply increases, similar to the results of Kim et al.[55] This improvement in the carrier mobility probably comes from grain growth of the material and a reduction in scattering centers during the high temperature treatment.[69] Grain growth in Bi_2Te_3 was directly observed and supported by Schultz et al.[59] No grain growth was observed in the bulk Bi_2Te_3 specimens at 325 °C, but grain growth was observed at 400 and 500 °C. Higher carrier mobility leads to larger electrical conductivity, which is consistent with our observations.

To verify the conjecture that annealing leads to a transition from p- to n-type semiconductor, the pristine Bi_2Te_3 powders were hot-pressed to bulk format at 500 °C in a N_2 environment and then measured at room temperature. Two hot press runs, one for 10 min and another for 3 h, generated bulk samples with densities of 6.1 g/cm^3 and 7.1 g/cm^3 (about 79% and 92% relative density), respectively. The thermoelectric and electrical properties of both samples agree. The higher density sample had an *S* of −108 μV/K and ρ of 0.58 mΩ cm while the other sample's properties were −90 μV/K and 0.6 mΩ cm, respectively. Compared with the positive *S* values from the SLM-produced samples, these results confirm high temperature annealing changed Bi_2Te_3 from a p-type to n-type semiconductor.

Figure 6(a) shows the measured specific heat and thermal diffusivity in the cross-plane direction; both properties increase with temperature. The thermal conductivity was then calculated according to them. The thermal conductivity increased with increasing temperature over the entire measurement region as shown in Fig. 6(b). With measured properties, the thermoelectric figure of merit *ZT* was calculated, as shown in Fig. 6(b). The behavior of *ZT* with temperature is primarily dominated by the electrical conductivity and the Seebeck coefficient. *ZT* first decreased with increasing temperature until about 300 °C, slightly increased between 300 and 400 °C, then increased more sharply with increasing temperature. The highest *ZT* value was about 0.11 at 50 °C. The *S* and *ZT* values of the SLM-processed bulk Bi_2Te_3 are in the same range as other p-type or doped n-type bulk samples.[70] These results indicate that the SLM method is capable of producing Bi_2Te_3 samples with thermoelectric properties comparable to samples produced by traditional methods.

IV. CONCLUSION

The results presented here demonstrate successful SLM of a thermoelectric material (Bi_2Te_3) from a loose powder. Even though the powder morphology made spreading of thin layers a challenge, loose powder was processed in a layer-by-layer approach to build a bulk solid without requiring any pre- or post-processing.

Although low relative density is a challenge for the SLM technique, effective selection of processing parameters enabled a final part relative density of 88%; pores on the surface and within the body of the parts were still evident. The structure and physical properties of the final bulk parts were fully characterized. SEM micrographs did not show separation between adjacent layers, suggesting sufficient melting within and between layers. The X-ray diffraction measurements confirmed the structure and the crystallographic preferred orientation of Bi_2Te_3 were conserved during the laser processing. The temperature-dependent Seebeck coefficient, electrical conductivity, specific heat, thermal diffusivity, and thermoelectric figure of merit *ZT* of the laser melted Bi_2Te_3 sample consistently indicated an evolution of defects, carriers, and mobility with temperature, and these property changes as a function of temperature explain the observed p- to n-type transition at around 350 °C. The SLM-produced Bi_2Te_3 bulk sample had similar thermoelectric and electrical properties to those fabricated from traditional methods. Although SLM of thermoelectric materials is nascent, this work attests to its viability and signals its applicability to other thermoelectric materials.

ACKNOWLEDGMENTS

We would like to acknowledge support from Oak Ridge National Laboratory Manufacturing Demonstration Facility RAMP-UP (Subcontract 4000145175), Virginia Center for Innovative Technology (CRCF Award MF16-020-En), and GWU University Facilitating Fund. We are especially grateful to James Ridenour and Dr. Christopher L. Cahill for equipment use and assistance with the XRD work, and we wish to acknowledge Linseis Inc. for the assistance of characterization of thermal and electrical properties. G.S.N. acknowledges support from the National Science Foundation Grant No. DMR-1748188. D.H. acknowledges support from the II-VI Foundation Block-Gift Program. Electron microscopy was conducted in The George Washington University Nanofabrication and Imaging Center.

REFERENCES

1. H.J. Goldsmid and R.W. Douglas: The use of semiconductors in thermoelectric refrigeration. *Br. J. Appl. Phys.* **5**, 386 (1954).
2. G.S. Nolas, J.L. Cohn, G.A. Slack, and S.B. Schujman: Semiconducting Ge clathrates: Promising candidates for thermoelectric applications. *Appl. Phys. Lett.* **73**, 178 (1998).
3. G.S. Nolas, D.T. Morelli, and T.M. Tritt: Skutterudites: A phonon-glass-electron crystal approach to advanced thermoelectric energy conversion applications. *Annu. Rev. Mater. Sci.* **29**, 89 (1999).
4. A. Purkayastha, F. Lupo, S. Kim, T. Borca-Tasciuc, and G. Ramanath: Low-temperature, template-free synthesis of single-crystal bismuth telluride nanorods. *Adv. Mater.* **18**, 496 (2006).
5. M.S. Dresselhaus, G. Chen, M.Y. Tang, R.G. Yang, H. Lee, D.Z. Wang, Z.F. Ren, J-P. Fleurial, and P. Gogna: New directions for low-dimensional thermoelectric materials. *Adv. Mater.* **19**, 1043 (2007).
6. T.M. Tritt: Thermoelectric phenomena, materials, and applications. *Annu. Rev. Mater. Res.* **41**, 433 (2011).
7. Y. Tang, R. Hanus, S. Chen, and G.J. Snyder: Solubility design leading to high figure of merit in low-cost Ce–$CoSb_3$ skutterudites. *Nat. Commun.* **6**, 7584 (2015).
8. M. Beekman, D.T. Morelli, and G.S. Nolas: Better thermoelectrics through glass-like crystals. *Nat. Mater.* **14**, 1182 (2015).
9. B. Dörling, J.D. Ryan, J.D. Craddock, A. Sorrentino, A. El Basaty, A. Gomez, M. Garriga, E. Pereiro, J.E. Anthony, M.C. Weisenberger, A.R. Goñi, C. Müller, and M. Campoy-Quiles: Photoinduced p- to n-type switching in thermoelectric polymer-carbon nanotube composites. *Adv. Mater.* **28**, 2782 (2016).
10. C.J.L. Hermes and J.R. Barbosa, Jr.: Thermodynamic comparison of Peltier, Stirling, and vapor compression portable coolers. *Appl. Energy* **91**, 51 (2012).
11. M.A. Karri, E.F. Thacher, and B.T. Helenbrook: Exhaust energy conversion by thermoelectric generator: Two case studies. *Energy Convers. Manage.* **52**, 1596 (2011).
12. S. LeBlanc: Thermoelectric generators: Linking material properties and systems engineering for waste heat recovery applications. *Sustainable Mater. Technol.* **1–2**, 26 (2014).
13. A.F. Ioffe, L.S. Stil'bans, E.K. Iordanishvili, T.S. Stavitskaya, A. Gelbtuch, and G. Vineyard: Semiconductor thermoelements and thermoelectric cooling. *Phys. Today* **12**, 42 (1959).
14. T.C. Harman, P.J. Taylor, D.L. Spears, and M.P. Walsh: Thermoelectric quantum-dot superlattices with high *ZT*. *J. Electron. Mater.* **29**, L1 (2000).
15. R. Venkatasubramanian, E. Siivola, T. Colpitts, and B. O'Quinn: Thin-film thermoelectric devices with high room-temperature figures of merit. *Nature* **413**, 597 (2001).
16. B. Poudel, Q. Hao, Y. Ma, Y. Lan, A. Minnich, B. Yu, X. Yan, D. Wang, A. Muto, D. Vashaee, X. Chen, J. Liu, M.S. Dresselhaus, G. Chen, and Z. Ren: High-thermoelectric performance of nanostructured bismuth antimony telluride bulk alloys. *Science* **320**, 634 (2008).
17. A.I. Hochbaum, R. Chen, R.D. Delgado, W. Liang, E.C. Garnett, M. Najarian, A. Majumdar, and P. Yang: Enhanced thermoelectric performance of rough silicon nanowires. *Nature* **451**, 163 (2008).
18. G. Zhang, Q. Yu, W. Wang, and X. Li: Nanostructures for thermoelectric applications: Synthesis, growth mechanism, and property studies. *Adv. Mater.* **22**, 1959 (2010).
19. K. Nielsch, J. Bachmann, J. Kimling, and H. Böttner: Thermoelectric nanostructures: From physical model systems towards nanograined composites. *Adv. Energy Mater.* **1**, 713 (2011).
20. G. Pennelli: Review of nanostructured devices for thermoelectric applications. *Beilstein J. Nanotechnol.* **5**, 1268 (2014).
21. C.R. Deckard: U.S. Patent No. US4863538 A, Method and apparatus for producing parts by selective sintering (1986).
22. D.D. Gu, W. Meiners, K. Wissenbach, and R. Poprawe: Laser additive manufacturing of metallic components: Materials, processes and mechanisms. *Int. Mater. Rev.* **57**, 133 (2012).
23. M. Schmid, A. Amado, and K. Wegener: Materials perspective of polymers for additive manufacturing with selective laser sintering. *J. Mater. Res.* **29**, 1824 (2014).
24. A. Zocca, P. Colombo, C.M. Gomes, and J. Günster: Additive manufacturing of ceramics: Issues, potentialities, and opportunities. *J. Am. Ceram. Soc.* **98**, 1983 (2015).
25. C.Y. Yap, C.K. Chua, Z.L. Dong, Z.H. Liu, D.Q. Zhang, L.E. Loh, and S.L. Sing: Review of selective laser melting: Materials and applications. *Appl. Phys. Rev.* **2**, 041101 (2015).

26. A. El-Desouky, A.L. Read, P.M. Bardet, M. Andre, and S. Leblanc: Selective laser melting of a bismuth telluride thermoelectric materials. In *Proc Solid Free Symp*, D. Bourell, ed. (Solid Freeform Fabrication Symposium, Austin, Texas, 2015), pp. 1043–1050.
27. A. El-Desouky, M. Carter, M.A. Andre, P.M. Bardet, and S. LeBlanc: Rapid processing and assembly of semiconductor thermoelectric materials for energy conversion devices. *Mater. Lett.* **185**, 598 (2016).
28. A. El-Desouky, M. Carter, M. Mahmoudi, A. Elwany, and S. LeBlanc: Influences of energy density on microstructure and consolidation of selective laser melted bismuth telluride thermoelectric powder. *J. Manuf. Process.* **25**, 411 (2017).
29. Y. Mao, Y. Yan, K. Wu, H. Xie, Z. Xiu, J. Yang, Q. Zhang, C. Uher, and X. Tang: Non-equilibrium synthesis and characterization of n-type $Bi_2Te_{2.7}Se_{0.3}$ thermoelectric material prepared by rapid laser melting and solidification. *RSC Adv.* **7**, 21439 (2017).
30. K. Wu, Y. Yan, J. Zhang, Y. Mao, H. Xie, J. Yang, Q. Zhang, C. Uher, and X. Tang: Preparation of n-type Bi_2Te_3 thermoelectric materials by non-contact dispenser printing combined with selective laser melting. *Phys. Status Solidi RRL* **11**, 1700067 (2017).
31. Y. Yan, H. Ke, J. Yang, C. Uher, and X. Tang: Fabrication and thermoelectric properties of n-type $CoSb_{2.85}Te_{0.15}$ using selective laser melting. *ACS Appl. Mater. Interfaces* **10**, 13669 (2018).
32. F. Kim, B. Kwon, Y. Eom, J.E. Lee, S. Park, S. Jo, S.H. Park, B-S. Kim, H.J. Im, M.H. Lee, T.S. Min, K.T. Kim, H.G. Chae, W.P. King, and J.S. Son: 3D printing of shape-conformable thermoelectric materials using all-inorganic Bi_2Te_3-based inks. *Nat. Energy* **3**, 301 (2018).
33. H.J. Goldsmid: Bismuth telluride and its alloys as materials for thermoelectric generation. *Materials* **7**, 2577 (2014).
34. R. Sehr and L.R. Testardi: The optical properties of p-type Bi_2Te_3–Sb_2Te_3 alloys between 2–15 microns. *J. Phys. Chem. Solids* **23**, 1219 (1962).
35. H. Zhang, C-X. Liu, X-L. Qi, X. Dai, Z. Fang, and S-C. Zhang: Topological insulators in Bi_2Se_3, Bi_2Te_3, and Sb_2Te_3 with a single Dirac cone on the surface. *Nat. Phys.* **5**, 438 (2009).
36. J. Martin, S. Erickson, G.S. Nolas, P. Alboni, T.M. Tritt, and J. Yang: Structural and transport properties of $Ba_8Ga_{16}Si_xGe_{30-x}$ clathrates. *J. Appl. Phys.* **99**, 044903 (2006).
37. J. Martin and G.S. Nolas: Apparatus for the measurement of electrical resistivity, Seebeck coefficient, and thermal conductivity of thermoelectric materials between 300 K and 12 K. *Rev. Sci. Instrum.* **87**, 015105 (2016).
38. H.C.H. Ho, I. Gilbson, and W.L. Cheung: Effects of energy density on morphology and properties of selective laser sintered polycarbonate. *J. Mater. Process. Technol.* **89–90**, 204 (1999).
39. J. Wilkes, Y. Hagedorn, W. Meiners, and K. Wissenbach: Additive manufacturing of ZrO_2–Al_2O_3 ceramic components by selective laser melting. *Rapid Prototyp. J.* **19**, 51 (2013).
40. P. Bertrand, F. Bayle, C. Combe, P. Goeuriot, and I. Smurov: Ceramic components manufacturing by selective laser sintering. *Appl. Surf. Sci.* **254**, 989 (2007).
41. L.X. Liu, I. Marziano, A.C. Bentham, J.D. Litster, E.T. White, and T. Howes: Effect of particle properties on the flowability of ibuprofen powders. *Int. J. Pharm.* **362**, 109 (2008).
42. N. Batista, A. El-Desouky, J. Crandall, S. Wang, J. Yang, and S. LeBlanc: *Informatics, Electron. Microsystems* (TechConnect Briefs, Washington, District of Columbia, 2017); pp. 166–169.
43. W.M. Haynes: *CRC Handbook of Chemistry and Physics*, 95th ed. (CRC Press, Boca Raton, FL, 2014); pp. 4–52.
44. K. Kempen, L. Thijs, E. Yasa, M. Badrossamay, W. Verheecke, and J-P. Kruth: Process optimization and microstructural analysis for selective laser melting of $AlSi_{10}Mg$. *Solid Freeform Fabr. Symp. Proc.* **22**, 484 (2011).
45. K. Monroy, J. Delgado, and J. Ciurana: Study of the pore formation on CoCrMo alloys by selective laser melting manufacturing process. *Procedia Eng.* **63**, 361 (2013).
46. S. Katayama, Y. Kawahito, and M. Mizutani: Elucidation of laser welding phenomena and factors affecting weld penetration and welding defects. *Phys. Procedia* **5**, 9 (2010).
47. J.Y. Lee, S.H. Ko, D.F. Farson, and C.D. Yoo: Mechanism of keyhole formation and stability in stationary laser welding. *J. Phys. D: Appl. Phys.* **35**, 1570 (2002).
48. C.B. Satterthwaite and R.W. Ure: Electrical and thermal properties of Bi_2Te_3. *Phys. Rev.* **108**, 1164 (1957).
49. L.D. Zhao, B-P. Zhang, J-F. Li, H.L. Zhang, and W.S. Liu: Enhanced thermoelectric and mechanical properties in textured n-type Bi_2Te_3 prepared by spark plasma sintering. *Solid State Sci.* **10**, 651 (2008).
50. M. Saleemi, M.S. Toprak, S. Li, M. Johnsson, M. Muhammed, G. Chen, C. Gatti, Y. Zhang, M. Rowe, M. Muhammed, X.Y. Chen, J.M. Liu, M.S. Dresselhaus, G. Chen, and Z.F. Ren: Synthesis, processing, and thermoelectric properties of bulk nanostructured bismuth telluride (Bi_2Te_3). *J. Mater. Chem.* **22**, 725 (2012).
51. C. Euvananont, N. Jantaping, and C. Thanachayanont: Effects of composition and preferred orientation on microstructure and thermoelectric properties of p-type $(Bi_xSb_{(1-x)})_2Te_3$ alloys. *Curr. Appl. Phys.* **11**, S246 (2011).
52. H.J. Goldsmid: The electrical conductivity and thermoelectric power of bismuth telluride. *Proc. Phys. Soc.* **71**, 633 (1958).
53. H. Zou, D.M. Rowe, and G. Min: Growth of p- and n-type bismuth telluride thin films by co-evaporation. *J. Cryst. Growth* **222**, 82 (2001).
54. L.M. Goncalves, P. Alpuim, G. Min, D.M. Rowe, C. Couto, and J.H. Correia: Optimization of Bi_2Te_3 and Sb_2Te_3 thin films deposited by co-evaporation on polyimide for thermoelectric applications. *Vacuum* **82**, 1499 (2008).
55. J-H. Kim, J-Y. Choi, J-M. Bae, M-Y. Kim, and T-S. Oh: Thermoelectric characteristics of n-type Bi_2Te_3 and p-type Sb_2Te_3 thin films prepared by co-evaporation and annealing for thermopile sensor applications. *Mater. Trans.* **54**, 618 (2013).
56. F.I. Vasenin: Termoelektricheskie svoistva splavov sistemy vismut-tellur. *Zh. Tekh. Fiz.* **25**, 397 (1955).
57. L. Ainsworth: Single crystal bismuth telluride. *Proc. Phys. Soc., London, Sect. B* **69**, 606 (1956).
58. G.S. Nolas, J. Sharp, and H.J. Goldsmid: *Thermoelectrics: Basic Principles and New Materials Developments* (Springer-Verlag Berlin Heidelberg, Berlin, Germany, 2001).
59. J.M. Schultz, J.P. McHugh, and W.A. Tiller: Effects of heavy deformation and annealing on the electrical properties of Bi_2Te_3. *J. Appl. Phys.* **33**, 2443 (1962).
60. W.R. George, R. Sharples, and J.E. Thompson: The sintering of bismuth telluride. *Proc. Phys. Soc.* **74**, 768 (1959).
61. R.G. Bernard: Processes involved in sintering. *Powder Metall.* **2**, 86 (1959).
62. G.R. Miller and C-Y. Li: Evidence for the existence of antistructure defects in bismuth telluride by density measurements. *J. Phys. Chem. Solids* **26**, 173 (1965).
63. J. Horák, K. Čermák, and L. Koudelka: Energy formation of antisite defects in doped Sb_2Te_3 and Bi_2Te_3 crystals. *J. Phys. Chem. Solids* **47**, 805 (1986).
64. J. Horák, J. Navrátil, and Z. Starý: Lattice point defects and free-carrier concentration in $Bi_{2+x}Te_3$ and $Bi_{2+x}Se_3$ crystals. *J. Phys. Chem. Solids* **53**, 1067 (1992).
65. P. Lošťák, Č. Drašar, D. Bachan, L. Beneš, and A. Krejčová: Defects in $Bi_2Te_{3-x}Se_x$ single crystals. *Radiat. Eff. Defects Solids* **165**, 211 (2010).
66. J. Bludská, I. Jakubec, Č. Drašar, P. Lošťák, and J. Horák: Structural defects in Cu-doped Bi_2Te_3 single crystals. *Philos. Mag.* **87**, 325 (2007).

67. C. Drasar, P. Lostak, and C. Uher: Doping and defect structure of tetradymite-type crystals. *J. Electron. Mater.* **39**, 2162 (2010).
68. A. Hashibon and C. Elsässer: First-principles density functional theory study of native point defects in Bi_2Te_3. *Phys. Rev. B* **84**, 144117 (2011).
69. D-H. Kim and G-H. Lee: Effect of rapid thermal annealing on thermoelectric properties of bismuth telluride films grown by co-sputtering. *Mater. Sci. Eng., B* **131**, 106 (2006).
70. D.A. Wright: Thermoelectric properties of bismuth telluride and its alloys. *Nature* **181**, 834 (1958).

Supplementary Material

To view supplementary material for this article, please visit https://doi.org/10.1557/jmr.2018.390.